Article

Numerical Investigation of the Production Behavior of Methane Hydrates under Depressurization Conditions Combined with Well-Wall Heating

Xuke Ruan [1,2,3], Xiao-Sen Li [1,2,3,*] and Chun-Gang Xu [1,2,3]

[1] Key Laboratory of Gas Hydrate, Guangzhou Institute of Energy Conversion, Chinese Academy of Sciences, Guangzhou 510640, China; ruanxk@ ms.giec.ac.cn (X.R.); xucg@ ms.giec.ac.cn (C.-G.X.)
[2] Guangzhou Center for Gas Hydrate Research, Chinese Academy of Sciences, Guangzhou 510640, China
[3] Guangdong Provincial Key Laboratory of New and Renewable Energy Research and Development, Guangzhou 510640, China
[*] Correspondence: lixs@ms.giec.ac.cn; Tel.: +86-20-8705-7037

Abstract: In this study, a 2D hydrate dissociation simulator has been improved and verified to be valid in numerical simulations of the gas production behavior using depressurization combined with a well-wall heating method. A series of numerical simulations were performed and the results showed that well-wall heating had an influence enhancing the depressurization-induced gas production, but the influence was limited, and it was even gradually weakened with the increase of well-wall heating temperature. Meanwhile, the results of the sensitivity analysis demonstrated the gas production depended on the initial hydrate saturation, initial pressure and the thermal boundary conditions. The supply of heat for hydrate dissociation mainly originates from the thermal boundaries, which control the hydrate dissociation and gas production by depressurization combined with well-wall heating. However, the effect of initial temperature on the gas production could be nearly negligible under depressurization conditions combined with well-wall heating.

Keywords: methane hydrate; gas production; depressurization; well-wall heating; numerical simulation

1. Introduction

In worldwide marine deposits and permafrost areas, a large amount of potentially producible natural gas is enclosed in ice-like solid hydrate reservoirs [1]. The natural gas hydrate resource has been considered as a potential strategic energy resource for the future [2,3]. Several efficient and feasible gas recovery methods for in-situ CH_4 recovery from the hydrate reservoirs have been proposed, such as hot water injection [4,5], in situ combustion [6,7], depressurization [8–11], inhibitor injection [12,13], CO_2 replacement [14,15] and the combined methods [16–20]. Using these technologies, extensive research on natural gas production from hydrate in field trials has been conducted within the last decade [21–25]. Natural gas has been successfully extracted by injection of hot water and by depressurization at the permafrost reservoir of the Mallik site in Northwest Canada [21]. The first offshore production test has been carried out in the Nankai Trough, Japan, the technical feasibility of the depressurization technique is confirmed [24] and this method appears to be the most promising and economic one [3,26].

The depressurization method is based on hydrates dissociation by reducing the wellbore pressure below the hydrate phase equilibrium pressure at a specified temperature, without any extra heat source introduced into the natural gas hydrate reservoir [27,28]. The depressurization-induced hydrate

dissociation is limited by heat transfer [17,29]. The results of experimental and numerical simulations have shown that in the process of the gas production by depressurization, the temperatures can significantly be reduced so as to the pore water probably freezes and the hydrate reforms [9,16,30–32]. Either the freezing pore water or the hydrate reformation can plug the flow channels, reducing the permeability of the hydrate reservoirs and further reducing the gas production [33,34]. In order to avoid the pore water freeze and the hydrate reformation, the depressurization combining with well-wall heating method has been proposed [17]. To assess the efficiency of the combined method, it is necessary to obtain a number of dissociation data and information in advanced.

Numerical analysis is an effective approach in modeling and simulating hydrate dissociation in porous media, many numerical models have been systematically developed to simulate natural gas production from hydrates and predict the possible behaviors [8,26,29,35–39]. Sung et al. [35] developed a three-dimensional, multi-phase flow finite-difference numerical model to evaluate the gas recovery performances with Kim-Bishnoi kinetic dissociation model. Their study characterized the flow factors and the flow mechanism under the conditions of increased in situ permeability. Based on the experimental results, Masuda et al. [40] developed a 3D two-phase (gas-water) flow, finite-difference numerical simulator to model hydrate dissociation by depressurization. In this simulator, the Kim-Bishnoi Equation was used to determine the dissociation rate and the permeability of hydrate-bearing sandstone was firstly assumed to be the function of hydrate saturation. Sun and Mohanty [41] developed a fully implicit 3D kinetic simulator to simulate formation and dissociation of methane hydrates in porous media. Four components (hydrate, methane, water, and salt) and five phases (hydrates, gas, aqueous-phase, ice, and salt precipitate) were considered in their simulation. The study indicated that increase of initial temperature, introduction of salt component into the system, and decrease of outlet pressure have a greater effect on hydrate dissociation. Moridis et al. [42] escalated the equation-of-state CH_4-Hydrate module (EOSHYDR) to a new code named TOUGH-Fx/Hydrate. By solving the coupled equations of mass and heat transfer, kinetic model, flow equations, this code can model the flow of gas and water, the non-isothermal gas release, phase behavior and heat transfer in natural gas hydrate-bearing complex geological media at any field class of hydrate accumulations. Reagan et al. [43] carried out numerical simulations on Class 2 and Class 3 hydrate production research for investigating the gas hydrate dissociation by depressurization with the numerical model TOUGH-Fx/Hydrate. Through the simulations, the model was verified to be valid for the simulation results being highly consistent with real field test, and the study also identified that the efficiency of depressurization-based on production strategies depend on the migration of fluids. In our previous investigations, a 2D axisymmetric finite-difference, fully implicit model was developed to investigate the gas production behavior of hydrate dissociation by depressurization in hydrate-bearing porous media [34,39]. Here, the numerical model is improved to clarify the hydrate dissociation characteristics of the depressurization combining with well-wall heating method in a cylindrical system. The sensitivity analysis and the gas production behavior are numerically studied by a fully coupled numerical code.

2. Mathematical Models

Falser et al. [17] conducted a series of small-scale experimental production tests on cylindrical samples with a high hydrate saturation to investigate the increased gas production from hydrate by depressurization and simultaneous heating of the production wellbore. The experiment conditions were summarized in Table 1, which were used as basic data in our numerical investigation of production behavior of methane hydrate dissociation under depressurization combining with well-wall heating.

For the simulation, as shown in Figure 1, the cylindrical hydrate-bearing sediment sample has a diameter of 180 mm and a height of 206 mm, the 2D axisymmetric sample is equally divided into nine blocks in the axial direction and 15 blocks in the radial direction. The production well as well as the well-wall heating is defined on the left of the axis of the sample. A no-slip boundary condition is

assumed for all the walls and the right side of the axis. The boundary temperature keeps constant. The physical parameters used in the numerical simulation are listed in Table 2.

Table 1. Properties of hydrate bearing sample from Falser et al. [17].

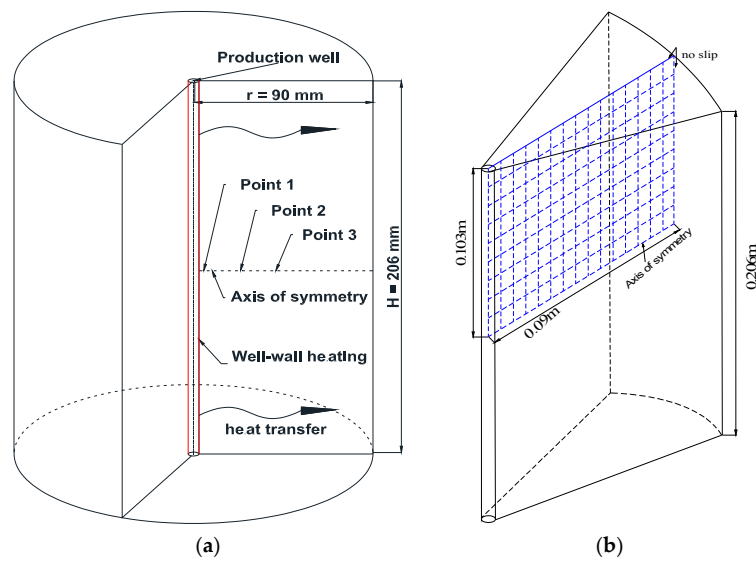| Variable	Value	Variable	Value
Sample length, L (mm)	206	Sample diameter, R (mm)	180
Initial pressure, P_0 (MPa)	14.44	Initial temperature, T_0 (K)	282.2
Heating temperature T_{well} (K)	288.15	Boundary temperature, T_b (K)	282.2
Intrinsic porosity, ϕ_0	0.378	Absolute permeability, k_0 (mD)	350
Hydrate saturation, S_{h0}	0.42	Environment temperature, T_E (K)	282.2
Water saturation, S_{w0}	0.50	Bottom-hole pressure, ΔP_{BHP} (MPa)	5.95
Gas saturation, S_{g0}	0.08	Permeability reduction exponent, N	10

Figure 1. Schematics of the (**a**) simulated region; and (**b**) the computational grid of hydrate dissociation.

Table 2. Physical parameters used in the numerical simulation.

Variable	Value		
Specific heat capacity (T = 293 K), C_p (J·kg^{-1}·K^{-1})	800 (sand) 500 (steel)	2010 (hydrate) 2157 (methane)	4189 (water) -
Thermal conductivity, k (W·m^{-1}·K^{-1})	3.92 (sand) 16 (steel)	0.62 (hydrate) 0.034 (methane)	0.56 (water) -
Density, ρ (g/cm^3)	2.60 (sand) 7.8 (steel)	0.90 (hydrate) 16 (methane, g/mol)	1.0 (water)
Cory parameters		n_w = 4	n_{gas} = 2
Viscosity (T = 293 K), μ (Pa·s)	0.001 (water)		1.25×10^{-5} (methane)
Phase equilibrium pressure, P_e (kPa)	$1.15 \times e^{49.3185 - 9459/T}$		
Cumulative gas production after 90min, V_{gas} (SL)	17 (experimental result of ΔP_6) [17]		
Cumulative gas production after 90min, V_{gas} (SL)	53 (experimental result of $\Delta P_6 + \Delta T$) [17]		

In our hydrate dissociation model, some assumptions have been made [8,27,28,34,39]: (1) the methane hydrate is deemed as sI type hydrate; (2) the methane gas produced from hydrate does not dissolve in water; (3) hydrate is assumed to accumulate in the pore space [34]; (4) gas-liquid two phase flow accords with Darcy's law; (5) the hydrate-bearing sediments are homogeneous and the solid phase (i.e., hydrate and porous media) is incompressible and stagnant.

2.1. Mass Conservation Equations

The cylindrical geometry is adopted in our mathematical models to present the relationships of the mass, the heat transfer and the hydrate dissociation reaction kinetics. The behavior of gas production and the pressure profile, the temperature profile are predicted in the process of hydrate dissociation and gas production under depressurization combining with well-wall heating.

The mass conservation Equations (1)–(3) describe the mass balance of gas, water and hydrate:

$$-\frac{1}{r}\frac{\partial}{\partial r}\left(r\rho_g v_{gr}\right) - \frac{\partial}{\partial x}\left(\rho_g v_{gx}\right) + \dot{q}_g + \dot{m}_g = \frac{\partial}{\partial t}\left(\phi\rho_g S_g\right) \tag{1}$$

$$-\frac{1}{r}\frac{\partial}{\partial r}\left(r\rho_w v_{wr}\right) - \frac{\partial}{\partial x}\left(\rho_w v_{wx}\right) + \dot{q}_w + \dot{m}_w = \frac{\partial}{\partial t}\left(\phi\rho_w S_w\right) \tag{2}$$

$$\dot{m}_h = \frac{\partial}{\partial t}\left(\phi\rho_h S_h\right) \tag{3}$$

where the subscripts "*g*", "*h*" and "*w*" refer to gas phase, hydrate phase and water phase, "*r*" represents the radial distance and "*x*" denotes the axis direction distance. v represents the Darcy velocity, ρ is the density, ϕ is the porosity of the hydrate-bearing sediments, and S means the saturation, which is defined as the fraction of the total pore volume in hydrate-bearing medium, $\dot{m}$ represents the mass rate produced from hydrate dissociation per unit volume, $\dot{q}$ represents the mass rate in terms of injection/production per unit volume. In this paper, the water phase is assumed to be incompressible, and the methane gas is assumed to meet the Pen-Robinson Equation of state.

The saturation of three components (gas, water and hydrate) follows the next relationship:

$$S_g + S_w + S_h = 1 \tag{4}$$

The Darcy velocities of gas and water in the mass conservation Equations (1) and (2) are described by the following equation, and the gravity force is ignored due to the laboratory-scale size in this study:

$$v_i = -\frac{Kk_{ri}}{\mu_i}\nabla P_i \quad (i = g, w) \tag{5}$$

where μ_i is the viscosity of the phase i, P_i is the pressure of the phase i, the relative permeability k_{rw} and k_{rg} are calculated using the Corey's model and expressed as follows:

$$k_{rw} = \left(\frac{\dfrac{S_w}{S_w + S_g} - S_{wr}}{1 - S_{wr} - S_{gr}}\right)^{n_w} \tag{6}$$

$$k_{rg} = \left(\frac{\dfrac{S_g}{S_w + S_g} - S_{gr}}{1 - S_{wr} - S_{gr}}\right)^{n_g} \tag{7}$$

where $n_w = 4$, $n_g = 2$, (as shown in Table 2) and the residual water saturation and gas saturation are given as $S_{wr} = 0.2$ and $S_{gr} = 0.3$.

In Equation (5), K is the absolutely permeability of hydrate-bearing porous media, which was firstly described in Masuda et al.'s model [40]. In the following Equation (8), K_0 is the original permeability without hydrate. N is a parameter called as the permeability reduction index, depending on the pore structure:

$$K = K_0(1 - S_h)^N \tag{8}$$

2.2. Energy Conservation Equations

In the energy conservation Equation (9), the following terms in turn are considered: such as heat conductive, convective heat transfer, heat input/output due to the injection/production of gas and water ($\dot{q}_g$ and $\dot{q}_w$), heat of hydrate dissociation $\dot{q}_h$ and heat transfer from surrounding $\dot{q}_{in}$. In the right hand side of equation is the change in terms of the enthalpy of the sand phase, hydrate phase, gas phase and water phase:

$$\frac{1}{r}\frac{\partial}{\partial r}\left(rk_c\frac{\partial T}{\partial r}\right) + \frac{\partial}{\partial x}\left(k_c\frac{\partial T}{\partial x}\right) - \frac{1}{r}\frac{\partial}{\partial r}\left(r\rho_g v_{gr}H_g + r\rho_w v_{wr}H_w\right) - \frac{\partial}{\partial x}\left(\rho_g v_{gx}H_g + \rho_w v_{wx}H_w\right)$$
$$+\dot{q}_g H_g + \dot{q}_w H_w + \dot{q}_h + \dot{q}_{in} = \frac{\partial}{\partial t}\left[(1-\phi)\rho_s H_s + \phi\left(S_h\rho_h H_h + S_g\rho_g H_g + S_w\rho_w H_w\right)\right] \tag{9}$$

$$k_c = (1-\phi)k_s + \phi\left(k_h S_h + k_w S_w + k_g S_g\right) \tag{10}$$

In Equation (9), h_i is the enthalpy for different phase i, and the subscript "s" means the sand phase. T is the local temperature, k_c is a function of local composition of the medium and represents the heat conductivity of hydrate-bearing sediments as expressed in Equation (10).

The heat of hydrate dissociation $\dot{q}_h$ can be calculated using the following expression:

$$\dot{q}_h = \dot{m}_h \Delta H_D \tag{11}$$

where ΔH_D presents the enthalpy change in hydrate dissociation, and can be defined as follows:

$$\dot{m}_g H_g + \dot{m}_w H_w + \dot{m}_h H_h = \dot{m}_h \Delta H_D \tag{12}$$

$$\Delta H_D = 446.12 \times 10^3 - 132.638T \tag{13}$$

$$dH_i = \frac{\partial H_i}{\partial T}dT + \frac{\partial H_i}{\partial P_i}dP_i = C_{pi}dT + \sigma_i dP_i \quad (i = h, g, w) \tag{14}$$

$$dH_s = \frac{\partial H_s}{\partial T}dT = C_{Ps}dT \tag{15}$$

In Equations (14) and (15), C_{pi} is the heat capacity, σ_i is the throttling coefficient for different phase i ($i = h, g, w$). The throttle coefficient of methane σ_g can be given as the Equation (16), based on the data of Tester [44]:

$$\sigma_g = \left(\frac{\partial H_g}{\partial P_g}\right)_T \approx -1.5 \times 10^{-4} \tag{16}$$

2.3. Kinetics Equations

According to the hydrate decomposition reaction, we can obtain the relationships as the following Equations:

$$\dot{m}_h = \dot{m}_g \frac{N_h M_w + M_g}{M_g} \tag{17}$$

$$\dot{m}_w = \dot{m}_g \frac{N_h M_w}{M_g} \tag{18}$$

where N_h are the coefficients of the decomposition reaction.

Based on the Kim-Bishnoi model of hydrate kinetics [45], the produced gas from hydrate can be calculated as follows:

$$\dot{m}_g = k_d M_g A_s(f_e - f) \tag{19}$$

where f and f_e are defined as gas fugacity and reaction balance fugacity, and in numerical simulation they are usually replaced by local gas pressure P_g and equilibrium pressure P_e, respectively.

In Equation (19), A_s is described as the interface area between hydrate and fluid phases, and it can be estimated by Amyx's method [46] as follows:

$$A_s = \sqrt{\frac{\phi_e^3}{2K}} \qquad (20)$$

$$\phi_e = \phi(1 - S_h) \qquad (21)$$

2.4. Initial and Boundary Conditions

In this study, the depressurization well as well as the location of well-wall heating is defined on the left of the simulated region, as shown in Figure 1. The on-slip boundary conditions are assumed for all the walls and the right side of the simulated region. The boundary condition for the ends of the simulated core is adiabatic. The initial conditions for the simulation are all shown in Table 1.

3. Comparison of Numerical Simulation with Experiment Data

In this work, the fully implicit numerical technique is used to simulate the hydrate dissociation in hydrate-bearing porous media under depressurization combined with well-wall heating. The numerical results of the cumulative gas production, the temperature and pressure vs. time are compared with the experimental results obtained by Falser et al. [17]. Tables 1 and 2 summarize the parameters used in this study. The cumulative gas production, the temperature and pressure obtained in the experiment and simulation with the numerical code are shown in Figures 2–4, respectively.
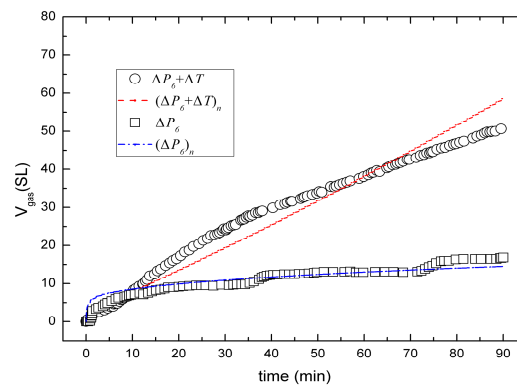

Figure 2. Comparison of the cumulative gas production obtained from the simulation results and the experimental data [17].
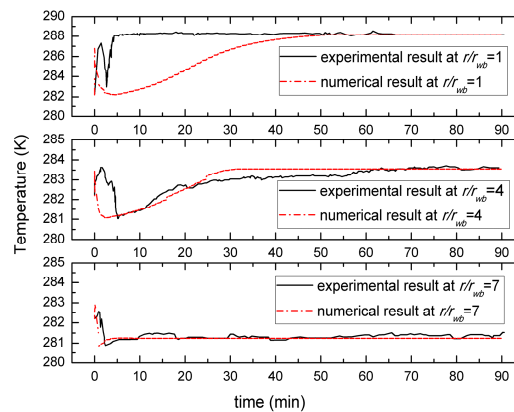

Figure 3. Temperature evolutions of $\Delta P_6 + \Delta T$ at different sections, experimental data [17] and numerical simulations are shown as solid lines and dashed lines, respectively.
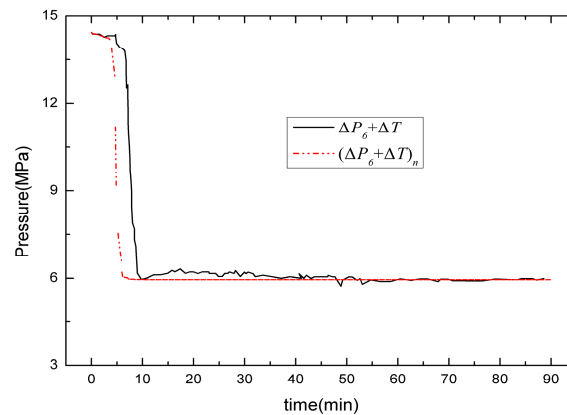
Figure 4. Simulation and experimental comparison of pressure variations during the hydrate dissociation of $\Delta P_6 + \Delta T$ in the production period.

Figure 2 shows that the comparison between the cumulative gas production obtained from the simulation and the experiment for two different hydrate dissociation cases. The two cases include: (1) the production pressure is depressurized to 5.95 MPa (approximately 6 MPa) without heating on production well walls, marked as ΔP_6, (2) depressurizing to 6 MPa and heating the well-wall from 282 to 288 K, marked as $\Delta P_6 + \Delta T$. All produced gas volumes are given in liters at standard conditions (SL). We can see that the numerical results (subscript n) support the production trends with the experimental data obtained from Falser et al. [17], the cumulative gas production after 90 min obtained from the numerical simulation is 15 and 58 SL for ΔP_6 and $\Delta P_6 + \Delta T$, respectively; while the experimental result is 17 SL for ΔP_6 and 53 SL for $\Delta P_6 + \Delta T$ (as shown in Table 2), and the mismatch can be attributed to the lack of some key experimental data, for example, the specific surface area of hydrate dissociation and the permeability are determined by empirical formulas, the actual distribution of hydrate is heterogeneous. The uncertain experimental data may have a significant effect on the numerical simulation of the process of hydrate dissociation.

Figure 3 shows the variations of temperature with time at three different positions of the cylindrical hydrate-bearing sediment sample, and the three measured positions are placed at radial distances $r/r_{wb} = 1, 4, 7$ wellbore radii from axis (the absolute distances are 5, 20, 35 mm from the axis). As shown in Figure 3, the numerical results agree well with the experimental data. The temperature curves of the depressurization combined with the well-wall heating show the temperature increases from a same initial temperature, then it decreases to a minimum, and then it will rebound to the environmental temperature or the heating temperature. This is due to that the hydrate dissociation is an endothermic process, which causes the temperature near the dissociation area to decrease. However, the heat transfer from the heating well-wall and the isothermal boundary environments can cause the temperature to increase.

The simulation and experimental results of pressure variations during the hydrate dissociation of $\Delta P_6 + \Delta T$ are plotted in Figure 4, the numerical results (subscript n) are shown in dashed-dotted lines and the experimental results are shown in solid lines. The wellbore pressure is kept constant during the gas production period. The mismatch between the numerical pressure profile and experimental pressure profile could be attributed to the lack of some key experimental data and the fluctuate in experimental operation for controlling the depressurization rate. From Figure 4, we can see the pressure reduces quickly to the wellbore pressure (5.95 MPa) from the initial high pressure (14.44 MPa), and the larger pressure difference leads to larger dissociation driving force for the hydrate dissociation in the presence of sufficient and available heat energy at the initial time.

4. Results and Discussion

Based on the comparison between the numerical results of the cumulative gas production, the temperature and pressure with the experimental data, Figure 2 indicate that the model is feasible to simulate the dissociation of methane hydrate under depressurization combining with well-wall heating.

In this section, we discuss the gas generation rate and temperature distribution of hydrate dissociated by depressurization combining with well-wall heating. The sensitivies of the initial hydrate saturation S_{h0}, the initial temperature T_0, the initial pressure P_0, and the boundary thermal conditions to hydrate dissociation have also been investigated.

4.1. Different Production Methods

Thermal simulation can be considered as a complement for gas production from hydrates by depressurization due to the limitation of sufficient and available heat energy in porous media [47]. In this work, the well-wall heating is adopted to combine with the depressurization method, the gas generation rate and temperature distribution of this method are compared with the cases of other production methods.

Figure 5 shows the gas generation rates during hydrate dissociation induced by well-wall heating method, depressurization, and depressurization combining with the well-wall heating method, respectively. The production period for each numerical simulation is 90 min, the production pressure is decreased from the initial high pressure (14.44 MPa) to the wellbore pressure (5.95 MPa) for both the depressurization method and the depressurization combining with well-wall heating method, the well-wall heating temperature is at 288.15 and 353.15 K for the combined method and the wall-heating method, respectively. As shown in Figure 5, we can see the gas generation rate of the combining depressurization with well-wall heating is higher than the case of depressurization and well-wall heating. Moreover, the gas generation rate of the combined method is better than those of the other two methods since from the production initial stage to 30 min. It indicates the effect of both the depressurization and well-wall heating driving forces on methane hydrate dissociation is quite obvious. Compared to the result of the depressurization method, it is clear that the additional well-wall heating is helpful to increase the gas production, and can supply much more heat to the hydrate dissociation.
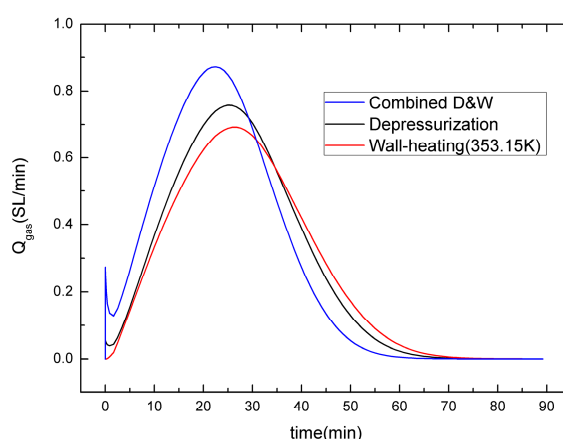

Figure 5. Gas generation rate during hydrate dissociation induced by different production methods.

For the temperature distribution of different production methods, the temperature distribution of depressurization combining with well-wall heating is significantly different from the case of depressurization (as shown in Figure 6). As presented in Table 1, the initial temperature is 282.2 K, which is same as the boundary temperature. For the temperature distribution of ΔP_6, the temperature

profile is simple. Like the temperature varieties at radial distances $r/r_{wb} = 1$ for a 90 min production period, the temperature decreases from 282.2 K to the minimum temperature 279.4 K, due to hydrate dissociation. Simultaneously, the temperature profiles at $r/r_{wb} = 4, 7$, respectively, decline accordingly as the hydrate dissociation goes on.
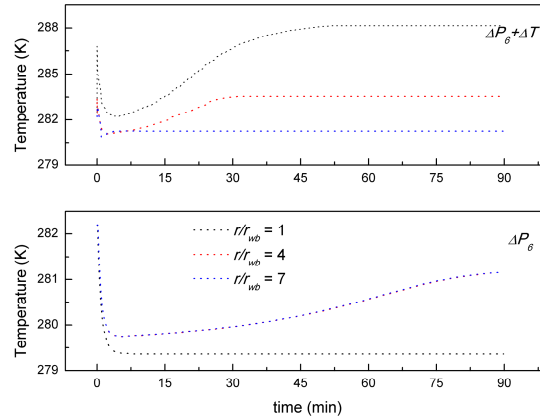

Figure 6. Temperature evolutions of $\Delta P_6 + \Delta T$ and ΔP_6 at different wellbore radii r/r_{wb} during production process.

Comparing with the temperature distribution of ΔP_6, the temperature distribution of $\Delta P_6 + \Delta T$ has a rapidly rise due to the additional thermal input, as shown in Figure 6. It seems that the rise of the temperature is caused by the heat transfer from well-wall heating. Simultaneously, the temperatures of depressurization combining with well-wall heating are different at different radial distances from axis ($r/r_{wb} = 1, 4, 7$), and the farther the distance from the well-wall the smaller and slower temperature increase. It indicates that the thermal conduction of well-wall heating is slow and the heat only transmits to a small dissociation area from wellbore. In addition, at the same time, the temperatures of $\Delta P_6 + \Delta T$ (at $r/r_{wb} = 1, 4$) go up again, in contrast, the temperatures of ΔP_6 just decrease because of hydrate dissociation, which indicates the hydrate dissociation of $\Delta P_6 + \Delta T$ is more faster than the case of ΔP_6, and it presents the well-wall heating improves the gas production of hydrate dissociation induced by depressurization.

4.2. Sensitivity to the Combining Well-Wall Heating Temperature

In the simulations of the depressurization combining well-wall heating, different well-wall heating temperatures (298.15, 323.15, and 353.15 K) have been adopted, and the numerical results of gas generation rate of the depressurization combining with different well-wall heating have been displayed in Figure 7. The gas generation rate increase with the increase of the combining well-wall heating temperature, the maximum gas generation rate is 0.94, 0.92, and 0.87 SL/min for the well-wall heating temperatures of 353.15, 323.15, and 298.15 K, respectively. As discussed in Section 4.1, the combined method has promoted the gas production. However, as shown in Figure 7, the difference between the gas generation rate decreases with the increase of well-wall heating temperature. This indicates the effect of the combined method on gas production gradually weakens with the increase of the well-wall heating temperature. For the reasons about the negative relationship of the gas production rate with the well-wall heating temperature, it is most likely due to the fact the production wellbore as well as the location of the well-wall heating is defined on the left as shown in Figure 1a, which indicates the heat is transferred from well-wall to the dissociation area, while the multi-phase fluid (gas and water) flows to the production well in the opposite direction. An amount of heat is actually removed by the produced gas/water, and its effect on hydrate dissociation diminishes greatly. Thus, a single wellbore may not be suitable for the gas production from hydrate using the depressurization combining with higher well-wall heating temperature.
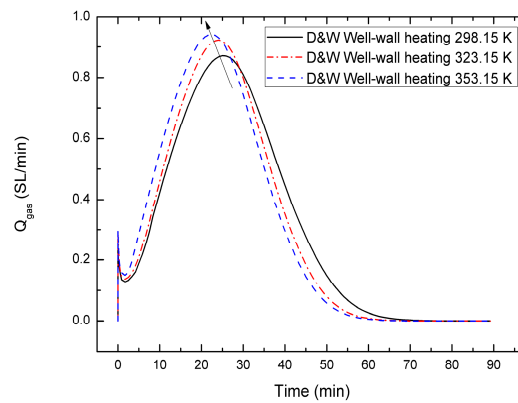
Figure 7. Gas generation rate of the depressurization combining with different well-wall heating temperature.

4.3. Sensitivity to the Initial Hydrate Saturation S_{h0}

For the case of depressurization combining with well-wall heating method, the evolutions of the gas generation rate over time with different initial hydrate saturation are plotted in Figure 8. The initial hydrate saturations are 0.3, 0.4 and 0.5, respectively. The initial water saturation is fixed at the value. As seen from Figure 8, a lower initial hydrate saturation leads to a higher gas generation rate, the maximum value of the three initial hydrate saturations (S_{h0} = 0.3, 0.4 and 0.5) is 0.92, 0.87 and 0.63 SL/min, respectively. One reason is the lower initial hydrate saturation means a higher initial gas saturation, and more free gas can be produced easily and quickly once the production wellbore opens. Another reason is the higher initial effective permeability in the lower S_{h0} leads to the faster depressurization, and hydrate dissociation will be earlier than the case of the higher S_{h0} in the gas production process.
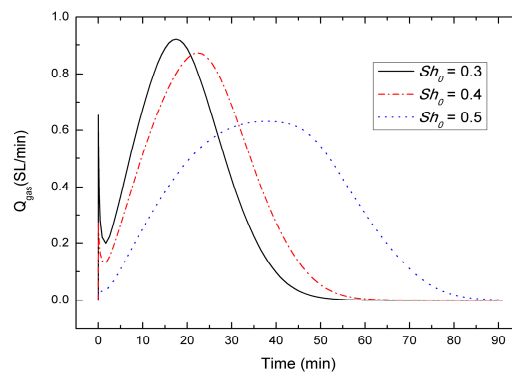

Figure 8. Gas generation rate with varying initial hydrate saturation.

Moreover, the end time of gas production for each case of S_{h0} (0.3, 0.4 and 0.5) is 50, 60 and nearly 90 min, respectively. The lower S_{h0} leads to the shorter continued time in a gas production process. Because of the faster average rate of fluid flow and the lower total quantity of hydrate in porous media at lower initial saturations.

4.4. Sensitivity to the Initial Pressure P_0

The simulations with different initial pressures of 13.44, 14.44 and 15.44 MPa are performed to investigate the sensitivity of the initial pressure P_0 to gas generation rate in the case of depressurization combining with well-wall heating. The other simulation conditions are same as those listed in Tables 1 and 2. As shown in Figure 9, the effect of initial pressure on gas generation rate is not

outstanding as the case of different initial hydrate saturations described in Section 4.3. Under lower initial pressure, more amount of gas has been generated at the early stage of the gas production process. It can be explained that the higher initial pressure causes a slower pressure drop, and a lower initial pressure can quickly reach to the equilibrium pressure P_e. Thus, we can see that the gas generation rate increases with the decrease of initial pressure, as shown in Figure 9.
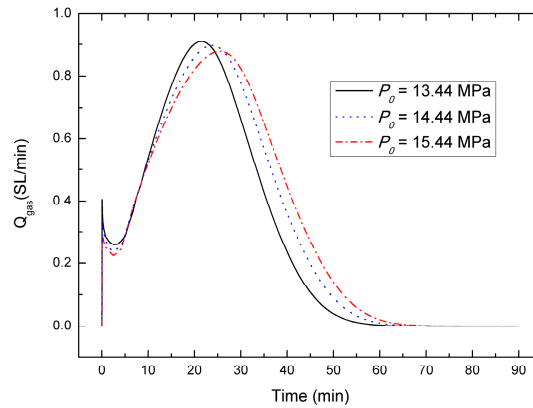

Figure 9. Gas generation rate with varying initial pressure.

4.5. Sensitivity to the Initial Temperature T_0

Several simulation runs are conducted to investigate the effect of initial temperature on gas generation rate in the case of depressurization combining with well-wall heating. The initial temperature varies from 276.2 to 288.2 K, by intervals of 6 K. As shown in Figure 10, the gas generation rate increases with the initial temperature. This is in contrast with the effect of initial pressure as described in Section 4.4. Meanwhile, the differences of the gas generation rate with various initial temperatures are slight and the effect of initial temperature on the gas production behavior could be nearly negligible, the result is also different with the issue of initial temperature affecting on the hydrate dissociation using depressurization [16,41]. A high initial temperature do not always have an important effect on gas production from hydrate using depressurization combining with well-wall heating, especially after its initial stage. It may be attributed to the additional thermal input from well-wall heating fulfilling the heat of hydrate dissociation.
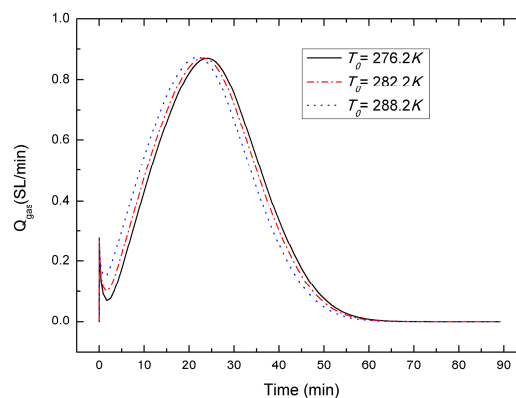

Figure 10. Gas generation rate with varying initial temperature

4.6. Sensitivity to the Thermal Boundary Conditions

In this section, in order to evaluate the effects of heat from surrounding boundaries, we perform a comparison simulation between normal boundary conditions and insulated boundary conditions.

The normal boundary is $T(L, t)$ = 282 K, while $\partial T(L, t)/\partial L = 0$ is used for the insulated boundary conditions. Based Equation (10), the averaged heat conductivity is around 2.81 W·m^{-1}·K^{-1} for this simulation.

Figure 11 shows the variations of the gas generation rate and the cumulative gas production under different boundary conditions. It's clear that the gas production behaviors depend strongly on the boundary thermal conditions, and the gas generation rate and the cumulative gas production are greatly reduced under the insulated boundary conditions, even the gas generation rate decreases to zero in a shorter time. Notably, none hydrates dissociate if it is lack of heat energy, for the reason that the thermal of well-wall heating only plays a role in a small dissociation area, the amount of heat received from the well-wall heating is small, and no heat transfers from insulated wall boundary to supply sufficient heat for hydrate dissociation reaction. Besides, the analysis of temperature distribution in Figures 3 and 6 (as described in Sections 4.1 and 4.2) also indicate the increase of temperature after the initial stage is attributed to the heat transfer from surrounding boundaries. Thus, we can see the heat for hydrate dissociation mainly originates from the boundaries, and the supply of heat from surrounding boundaries controls the hydrate dissociation and gas production. It also indicates that the depressurization combining with well-wall heating method may be unfeasible for the hydrate exploitation in a surrounding with lower temperature.
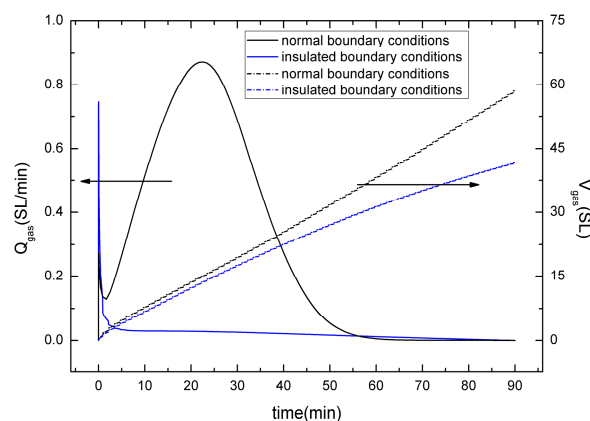

Figure 11. Gas generation rate and cumulative gas production time evolution for the normal boundary conditions and insulated boundary conditions.

5. Conclusions

In this work, a 2D axisymmetric simulator of hydrate dissociation is improved and verified to be valid in numerical simulation of the gas production behaviors using the depressurization combining with well-wall heating method. The sensitivies of the well-heating temperature, the initial hydrate saturation S_{h0}, the initial temperature T_0 and pressure P_0, and the boundary thermal conditions to the gas production have been discussed. On the basis of the presented results, the following conclusions can be drawn:

(1) The temperature distribution of depressurization combined with well-wall heating is significantly different from the case of depressurization. In the case of depressurization combined with well-wall heating, the temperature increases from the same initial temperature, then it decreases to a minimum, and then it will rebound to the environmental temperature or the heating temperature. In a word, the temperature shows a rapid increase due to the additional thermal input, however, the depressurization temperature is decreased from the initial value to the minimum.

(2) Comparing with the gas production behaviors of the depressurization, well-wall heating and depressurization combined with well-wall heating method, the well-wall heating is benefit to

increase the gas production, and the gas generation rate of the depressurization combined with well-wall heating method is highest, followed by the other cases. Meanwhile, owing to the fact that the thermal conduction of well-wall heating is slow and the heat transmits only to a small dissociation area, the influence of the well-wall heating on gas production is limited, even is gradually weakened with an increasing well-wall heating temperature. A single wellbore may not be suitable for the gas production from hydrate using the depressurization combined with higher well-wall heating temperature.

(3)   For the depressurization combined with well-wall heating method, a lower initial hydrate saturation leads to a higher gas generation rate, the gas generation rate increases with the decrease of initial pressure, and in contrast with the effect of initial hydrate saturation and initial pressure, the effect of initial temperature on the gas production behavior could be nearly negligible, which is different from the case of other production method.

(4)   For the depressurization combined with well-wall heating method, the gas production strongly depends on the heat originating from the boundaries, the supply of heat from surrounding boundaries controls the hydrate dissociation and gas production. The depressurization combined with well-wall heating method may be unfeasible for the hydrate exploitation in a surrounding with lower temperature.

Author Contributions: Xuke Ruan developed the numerical simulation code and carried out numerical simulations; Xuke Ruan and Xiao-Sen Li analyzed the numerical data and evaluated the numerical results; Xuke Ruan and Chun-Gang Xu wrote the paper.

Conflicts of Interest: The authors declare no competing financial interest.

Nomenclature

A_s	specific surface area of porous medium bearing gas hydrate (m^2)
C_p	specific heat capacity (J·kg^{-1}·K^{-1})
C_{ps}	heat capacity of porous media (J·kg^{-1}·K^{-1})
C_{pg}	heat capacity of gas (J·kg^{-1}·K^{-1})
C_{pw}	heat capacity of water (J·kg^{-1}·K^{-1})
C_{ph}	heat capacity of hydrate (J·kg^{-1}·K^{-1})
f_e	fugacity of gas at the hydrate equilibrium pressure corresponding to the local temperature
f	fugacity of gas under the local temperature and pressure
ΔH_D	the enthalpy change in hydrate dissociation (J·kg^{-1})
H_g	enthalpy of gas (J·kg^{-1})
H_w	enthalpy of water (J·kg^{-1})
H_h	enthalpy of hydrate (J·kg^{-1})
H_s	enthalpy of porous media (J·kg^{-1})
k	thermal conductivity (W·m^{-1}·K^{-1})
k_c	thermal conductivity coefficient of hydrate-bearing medium (W·m^{-1}·K^{-1})
k_g	thermal conductivity coefficient of gas (W·m^{-1}·K^{-1})
k_w	thermal conductivity coefficient of water (W·m^{-1}·K^{-1})
k_h	thermal conductivity coefficient of hydrate (W·m^{-1}·K^{-1})
k_s	thermal conductivity coefficient of porous media (W·m^{-1}·K^{-1})
K	absolute permeability (mD)
K_0	original permeability without hydrate (mD)
k_0	initial absolute permeability (mD)
k_d	dissociation rate constant (mol/(m^2·Pa·s))

k_{rg}	relative permeability of gas phase
k_{rw}	relative permeability of water phase
L	sample length (mm)
$\dot{m}_g$	mass rate of gas generated by hydrate dissociation per unit volume (kg/(m^3·s))
$\dot{m}_w$	mass rate of water generated by hydrate dissociation per unit volume (kg/(m^3·s))
$\dot{m}_h$	mass rate by hydrate dissociated per unit volume (kg/(m^3·s))
M_g	molecular weight of gas (kg/kmol)
M_w	molecular weight of water (kg/kmol)
N_h	hydrate number
n_w	empirical constant ($n_w = 4$)
n_g	empirical constant ($n_g = 2$)
N	permeability reduction index
P	pressure (Pa)
P_e	equilibrium pressure (Pa)
P_g	gas pressure (Pa)
P_w	water pressure (Pa)
P_0	initial pressure (Pa)
ΔP_{BHP}	bottom-hole pressure (Pa)
ΔP_6	production pressure depressurized to 5.95 MPa
$\Delta P_6 + \Delta T$	production pressure depressurized to 5.95 MPa with the well-wall heating
$\dot{q}_g$	mass rate in terms of injection/production of gas (kg/(m^3·s))
$\dot{q}_w$	mass rate in terms of injection/production of water (kg/(m^3·s))
$\dot{q}_h$	heat of hydrate decomposition unit bulk volume (J/(m^3·s))
$\dot{q}_{in}$	heat from the surroundings (J/(m^3·s))
R	sample diameter (mm)
S_g	hydrate saturation
S_w	water saturation
S_h	gas saturation
S_{gr}	residual gas saturation
S_{wr}	irreducible water saturation
T	system temperature (K)
T_0	initial temperature (K)
T_b	boundary temperature (K)
T_E	environment temperature (K)
T_{well}	well-wall heating temperature (K)
t	time (s)
v_{gr}	velocity of gas in r-direction (m/s)
v_{gx}	velocity of gas in x-direction (m/s)
v_{wr}	velocity of water in r-direction (m/s)
v_{wx}	velocity of water in x-direction (m/s)
x	axial distance
g	gas
w	water
r	radial distance
s	porous media
ϕ	porosity
σ_I	throttling coefficient for the i phase
ρ_g	density of gas (kg/m^3)
ρ_w	density of water (kg/m^3)
μ_g	viscosity of gas (Pa·s)
μ_w	viscosity of water (Pa·s)

References

1. Sloan, E.D.; Koh, C.A. *Clathrate Hydrates of Natural Gases*, 3rd ed.; CRC Press: Boca Raton, FL, USA, 2008.
2. Makogon, Y.F.; Holditch, S.A.; Makogon, T.Y. Natural gas-hydrates—A potential energy source for the 21st century. *J. Pet. Sci. Eng.* **2007**, *56*, 14–31. [CrossRef]
3. Moridis, G.J.; Collett, T.S.; Boswell, R.; Kurihara, M.; Reagan, M.T.; Koh, C.; Sloan, E.D. Toward production from gas hydrates: Current status, assessment of resources, and simulation-based evaluation of technology and potential. *SPE Reserv. Eval. Eng.* **2009**, *12*, 745–771. [CrossRef]
4. Tang, L.G.; Xiao, R.; Huang, C.; Feng, Z.P.; Fan, S.S. Experimental investigation of production behavior of gas hydrate under thermal stimulation in unconsolidated sediment. *Energy Fuels* **2005**, *19*, 2402–2407. [CrossRef]
5. Li, X.S.; Yang, B.; Li, G.; Li, B.; Zhang, Y.; Chen, Z.Y. Experimental study on gas production from methane hydrate in porous media by huff and puff method in pilot-scale hydrate simulator. *Fuel* **2012**, *94*, 486–494. [CrossRef]
6. Castellani, B.; Rossetti, G.; Tupsakhare, S.; Rossi, F.; Nicolini, A.; Castaldi, M.J. Simulation of CO_2 storage and methane gas production from gas hydrates in a large scale laboratory reactor. *J. Pet. Sci. Eng.* **2016**, *147*, 515–527. [CrossRef]
7. Castaldi, M.J.; Zhou, Y.; Yegulalp, T.M. Down-hole combustion method for gas production from methane hydrates. *J. Pet. Sci. Eng.* **2007**, *56*, 176–185. [CrossRef]
8. Sun, X.; Nanchary, N.; Mohanty, K.K. 1-D modeling of hydrate depressurization in porous media. *Transp. Porous Media* **2005**, *58*, 315–338. [CrossRef]
9. Moridis, G.; Kowalsky, M.; Pruess, K. Depressurization-induced gas production from Class 1 hydrate deposits. *SPE Reserv. Eval. Eng.* **2007**, *10*, 458–481. [CrossRef]
10. Konno, Y.; Masuda, Y.; Akamine, K.; Naiki, M.; Nagao, J. Sustainable gas production from methane hydrate reservoirs by the cyclic depressurization method. *Energy Convers. Manag.* **2016**, *108*, 439–445. [CrossRef]
11. Zhang, L.X.; Zhao, J.F.; Dong, H.S.; Zhao, Y.C.; Liu, Y.; Zhang, Y.; Song, Y.C. Magnetic resonance imaging for in-situ observation of the effect of depressurizing range and rate on methane hydrate dissociation. *Chem. Eng. Sci.* **2016**, *144*, 135–143. [CrossRef]
12. Kawamura, T.; Sakamoto, Y.; Ohtake, M.; Yamamoto, Y.; Haneda, H.; Yoon, J.H.; Komai, T. Dissociation behavior of hydrate core sample using thermodynamic inhibitor. *Int. J. Offshore Polar Eng.* **2006**, *16*, 5–9.
13. Li, G.; Li, X.S.; Tang, L.G.; Zhang, Y. Experimental investigation of production behavior of methane hydrate under ethylene glycol injection in unconsolidated sediment. *Energy Fuels* **2007**, *21*, 3388–3393. [CrossRef]
14. Ersland, G.; Huseb, J.; Graue, A.; Baldwin, B.A.; Howard, J.; Stevens, J. Measuring gas hydrate formation and exchange with CO_2 in Bentheim sandstone using MRI tomography. *Chem. Eng. J.* **2010**, *158*, 25–31. [CrossRef]
15. Xu, C.G.; Cai, J.; Lin, F.H.; Chen, Z.Y.; Li, X.S. Raman analysis on methane production from natural gas hydrate by carbon dioxide-methane replacement. *Energy* **2015**, *79*, 111–116. [CrossRef]
16. Li, G.; Moridis, G.J.; Zhang, K.; Li, X.-S. Evaluation of gas production potential from marine gas hydrate deposits in Shenhu area of South China Sea. *Energy Fuels* **2010**, *24*, 6018–6033. [CrossRef]
17. Falser, S.; Uchida, S.; Palmer, A.C.; Soga, K.; Tan, T.S. Increased gas production from hydrates by combining depressurisation with heating of the wellbore. *Energy Fuels* **2012**, *26*, 6259–6267. [CrossRef]
18. Yang, S.; Lang, X.; Wang, Y.; Wen, Y.; Fan, S. Numerical simulation of Class 3 hydrate reservoirs exploiting using horizontal well by depressurization and thermal co-stimulation. *Energy Convers. Manag.* **2014**, *77*, 298–305. [CrossRef]
19. Feng, J.C.; Wang, Y.; Li, X.S.; Li, G.; Zhang, Y.; Chen, Z.Y. Production performance of gas hydrate accumulation at the GMGS2-site 16 of the Pearl River mouth basin in the South China Sea. *J. Nat. Gas Sci. Eng.* **2015**, *27*, 306–320. [CrossRef]
20. Song, Y.; Wang, J.; Liu, Y.; Zhao, J. Analysis of heat transfer influences on gas production from methane hydrates using a combined method. *Int. J. Heat Mass Transf.* **2016**, *92*, 766–773. [CrossRef]
21. Dallimore, S.R.; Collett, T.S.; Taylor, A.E.; Uchida, T.; Weber, M.; Chandra, A.; Mroz, T.H.; Caddel, E.M.; Inoue, T. *Scientific Results from the Mallik 2002 Gas Hydrate Production Research Well Program, Mackenzie Delta, Northwest Territories, Canada*; Bulletin 585; Geological Survey of Canada: Qttawa, ON, Canada, 2005.

22. Anderson, B.J.; Kurihara, M.; White, M.D.; Moridis, G.J.; Wilson, S.J.; Pooladi-Darvish, M.; Gaddipati, M.; Masuda, Y.; Collett, T.S.; Hunter, R.B.; et al. Regional long-term production modeling from a single well test, Mount Elbert gas hydrate stratigraphic test well, Alaska North Slope. *Mar. Pet. Geol.* **2011**, *28*, 493–501. [CrossRef]

23. Moridis, G.J.; Silpngarmlert, S.; Reagan, M.T.; Collett, T.; Zhang, K. Gas production from a cold, stratigraphically-bounded gas hydrate deposit at the Mount Elbert gas hydrate stratigraphic test well, Alaska North Slope: Implications of uncertainties. *Mar. Pet. Geol.* **2011**, *28*, 517–534. [CrossRef]

24. Yamamoto, K. Overview and introduction: Pressure core-sampling and analyses in the 2012–2013 MH21 offshore test of gas production from methane hydrates in the Eastern Nankai Trough. *Mar. Pet. Geol.* **2015**, *66*, 296–309. [CrossRef]

25. Li, X.S.; Xu, C.G.; Zhang, Y.; Ruan, X.K.; Li, G.; Wang, Y. Investigation into gas production from natural gas hydrate: A review. *Appl. Energy* **2016**, *172*, 286–322. [CrossRef]

26. Kurihara, M.; Sato, A.; Ouchi, H.; Narita, H.; Masuda, Y.; Saeki, T.; Fujii, T. Prediction of gas productivity from Eastern Nankai Trough methane-hydrate reservoirs. *SPE Reserv. Eval. Eng.* **2009**, *12*, 477–499. [CrossRef]

27. Liang, H.; Song, Y.; Chen, Y. Numerical simulation for laboratory-scale methane hydrate dissociation by depressurization. *Energy Convers. Manag.* **2010**, *51*, 1883–1890. [CrossRef]

28. Ruan, X.; Song, Y.; Zhao, J.; Liang, H.; Yang, M.; Li, Y. Numerical simulation of methane production from hydrates induced by different depressurizing approaches. *Energies* **2012**, *5*, 438–458. [CrossRef]

29. Gerami, S.; Pooladi-Darvish, M. Predicting gas generation by depressurization of gas hydrates where the sharp-interface assumption is not valid. *J. Pet. Sci. Eng.* **2007**, *56*, 146–164. [CrossRef]

30. Li, X.S.; Zhang, Y.; Li, G.; Chen, Z.Y.; Wu, H.J. Experimental investigation into the production behavior of methane hydrate in porous sediment by depressurization with a novel three-dimensional cubic hydrate simulator. *Energy Fuels* **2011**, *25*, 4497–4505. [CrossRef]

31. Seol, Y.; Myshakin, E. Experimental and numerical observations of hydrate reformation during depressurization in a core-scale reactor. *Energy Fuels* **2011**, *25*, 1099–1110. [CrossRef]

32. Falser, S. *Gas Production from Methane Hydrate Bearing Sediments*; National University of Singapore: Singapore, 2012.

33. Seol, Y.; Kneafsey, T.J. Methane hydrate induced permeability modification for multiphase flow in unsaturated porous media. *J. Geophys. Res.* **2011**, *116*. [CrossRef]

34. Ruan, X.; Yang, M.; Song, Y.; Liang, H.; Li, Y. Numerical studies of hydrate dissociation and gas production behavior in porous media during depressurization process. *J. Nat. Gas Chem.* **2012**, *21*, 381–392. [CrossRef]

35. Sung, W.M.; Huh, D.G.; Ryu, B.J.; Lee, H.S. Development and application of gas hydrate reservoir simulator based on depressurizing mechanism. *Korean J. Chem. Eng.* **2000**, *17*, 344–350. [CrossRef]

36. Moridis, G.J. Numerical studies of gas production from Class 2 and Class 3 hydrate accumulations at the Mallik Site, Mackenzie Delta, Canada. *SPE Reserv. Eval. Eng.* **2004**, *7*, 175–183. [CrossRef]

37. Liu, Y.; Strumendo, M.; Arastoopour, H. Simulation of methane production from hydrates by depressurization and thermal stimulation. *Ind. Eng. Chem. Res.* **2009**, *48*, 2451–2464. [CrossRef]

38. Konno, Y.; Masuda, Y.; Hariguchi, Y.; Kurihara, M.; Ouchi, H. Key factors for depressurization-induced gas production from oceanic methane hydrates. *Energy Fuels* **2010**, *24*, 1736–1744. [CrossRef]

39. Ruan, X.; Song, Y.; Liang, H.; Yang, M.; Dou, B. Numerical simulation of the gas production behavior of hydrate dissociation by depressurization in hydrate-bearing porous medium. *Energy Fuels* **2012**, *26*, 1681–1694. [CrossRef]

40. Masuda, Y.; Fujinaga, Y.; Naganawa, S.; Fujita, H.; Sato, T.; Hayashi, Y. Modeling and experimental studies on dissociation of methane gas hydrates in Berea sandstone cores. In Proceedings of the 3rd Internatinal Conference on Gas Hydrates, Salt Lake City, UT, USA, 18–22 July 1999.

41. Sun, X.F.; Mohanty, K.K. Kinetic simulation of methane hydrate formation and dissociation in porous media. *Chem. Eng. Sci.* **2006**, *61*, 3476–3495. [CrossRef]

42. Moridis, G.J.; Kowalsky, M.B.; Pruess, K. *TOUGH + Hydrate v1.0.1 User's Manual: A Code for the Simulation of System Behavior in Hydrate-Bearing Geologic Media*; Lawrence Berkeley National Laboratory: Berkeley, CA, USA, 2005.

43. Reagan, M.T.; Moridis, G.J.; Zhang, K. Sensitivity analysis of gas production from Class 2 and Class 3 hydrate deposits. In Proceedings of the Offshore Technology Conference (OTC), Houston, TX, USA, 5–8 May 2008.

44. Tester, J.W.; Modell, M. *Thermodynamics and Its Applications*; Prentice Hall: Upper Saddle River, NJ, USA, 1997.

45. Kim, H.; Bishnoi, P.; Heidemann, R.; Rizvi, S. Kinetics of methane hydrate decomposition. *Chem. Eng. Sci.* **1987**, *42*, 1645–1653. [CrossRef]

46. Amyx, J.W.; Bass, D.M.; Whiting, R.L. *Petroleum Reservoir Engineering*; McGraw-Hill Book Company: New York, NY, USA, 1960.

47. Su, Z.; Huang, L.; Wu, N.; Yang, S. Effect of thermal stimulation on gas production from hydrate deposits in Shenhu area of the South China Sea. *Sci. China Earth Sci.* **2013**, *56*, 601–610. [CrossRef]